

Intergranular stress distributions in polycrystalline aggregates of irradiated stainless steel

J. Hure^{a,*}, S. El Shawish^b, L. Cizelj^b, B. Tanguy^a

^aCEA, Université Paris-Saclay, DEN, Service d'Études des Matériaux Irradiés, 91191 Gif-sur-Yvette cedex, France

^bJožef Stefan Institute, SI-1000, Ljubljana, Slovenia

Abstract

In order to predict InterGranular Stress Corrosion Cracking (IGSCC) of post-irradiated austenitic stainless steel in Light Water Reactor (LWR) environment, reliable predictions of intergranular stresses are required. Finite elements simulations have been performed on realistic polycrystalline aggregate with a recently proposed physically-based crystal plasticity constitutive equations validated for neutron-irradiated austenitic stainless steel. Intergranular normal stress probability density functions are found with respect to plastic strain and irradiation level, for uniaxial loading conditions. In addition, plastic slip activity jumps at grain boundaries are also presented. Intergranular normal stress distributions describe, from a statistical point of view, the potential increase of intergranular stress with respect to the macroscopic stress due to grain-grain interactions. The distributions are shown to be well described by a master curve once rescaled by the macroscopic stress, in the range of irradiation level and strain considered in this study. The upper tail of this master curve is shown to be insensitive to free surface effect, which is relevant for IGSCC predictions, and also relatively insensitive to small perturbations in crystallographic texture, but sensitive to grain shapes.

Keywords: Stress corrosion cracking, Irradiation hardening, Crystal plasticity, Finite element simulations

1. Introduction

Internals structures of Light Water Reactors (LWR) are made mainly of austenitic stainless steels, known for their good mechanical properties such as ductility and toughness, and their resistance to corrosion. Under neutron irradiation, a degradation of these properties is observed, such as a drastic decrease of fracture toughness and a susceptibility to stress corrosion cracking (SCC) [1, 2, 3]. This last phenomenon is referring to as Irradiation Assisted Stress Corrosion Cracking (IASCC), as it affects materials under irradiation initially non-sensitive to SCC. IASCC has been observed since the 1980's in both Boiling Water Reactors (BWR) and Pressurized Water Reactors (PWR), with the appearance of intergranular cracks for example in core shrouds in BWRs and baffle-to-former bolts in PWRs [4, 5]. Several researches have been conducted since then to assess the key parameters affecting both initiation and propagation of intergranular cracks in LWR's environment, parameters than can be divided into three groups: stress level [2, 6, 7, 8, 9], mechanical behaviour of the material and its chemical composition (which includes initial microstructure and chemical composition, and irradiated defects and segregation [10]), and LWR's environment [11, 12].

In recent years, different models have been proposed to predict IASCC of austenitic stainless steels, or more generally InterGranular Stress Corrosion Cracking (IGSCC). In some studies, slip localization, *i.e.* strongly heterogeneous deformation field at the grain scale has been argued to be responsible for IGSCC crack initiation, leading to models based on dislocation pile-up theory or refined slip bands modelling [13].

*Corresponding author

Other recent studies of SCC cracking are based on simulations of polycrystalline aggregates with cohesive zone models [14], leading to both prediction of initiation and propagation. These models using standard crystal plasticity constitutive equations assume implicitly that rather homogeneous deformation field at the grain scale can be sufficient to assess intergranular cracking. Such models have been used for example to predict SCC of Zircaloy in iodine environment [15] or SCC of cold-worked austenitic steels [16]. These fully coupled models require both an accurate crystal plasticity constitutive law and grain boundaries modelling in order to provide quantitative predictions. As crystal plasticity models are only recently available in the literature for irradiated materials [17, 18], and especially irradiated stainless steels [19, 20, 21], such simulations have not yet been performed so far for irradiated stainless steel.

These fully coupled models show some drawbacks such as high computational cost due to crack propagation and rather inaccurate intergranular stress prediction due to cohesive zone modeling [22]. Therefore, an intermediate approach is considered here following the work of Diard *et al.* [23, 24], based on the computation of accurate intergranular (normal) stress distributions for irradiated stainless steels for uncracked polycrystalline aggregate, as normal stress at grain boundaries is assumed to be the key parameter for intergranular cracking. Contrary to other studies [23, 25] focusing on relations between intergranular stress and orientation of the boundary with respect to the loading direction or to the mismatch of deformations between adjacent grains, full distributions for statistically large number of grains with different orientations are assessed. Combined with an empirical or experimental criterion for grain boundary strength that may depend on oxidation time and irradiation level, such uncoupled modelling could in principle be an efficient tool to predict critical macroscopic stress above which intergranular cracks are expected to be initiated at the grain scale, or intergranular surface cracking density. This approach is particularly relevant in the case of SCC of post-irradiated or heavily cold-worked austenitic stainless steel [26] in PWR nominal environment (compared to BWR oxygenated environment), where low propagation rates enables rather weak interactions between intergranular cracks, and thus the appearance of numerous surface cracks, as shown for example in [10] and [27], for neutron-irradiated and proton-irradiated stainless steel, respectively.

In the first part of the paper, recently proposed crystal plasticity physically-based constitutive equations for neutron-irradiated austenitic stainless steel [20, 21] that have been used in this study are described. In a second part, polycrystalline simulations based on a realistic aggregate are presented, leading to the stress distributions at grain boundaries as a function of strain and irradiation level. The effects of free surface, deviations from random crystallographic texture and equiaxed grain shapes are assessed. As a conclusion, and based on these numerical results, a methodology is proposed to obtain a statistical modelling of IGSCC initiation. The range of validity of such modelling is finally discussed.

2. Numerical modelling

2.1. Crystal plasticity constitutive model

A degradation of mechanical properties of irradiated austenitic stainless steels is commonly ascribed to the formation of high density nano-sized irradiation defect clusters, mainly interstitial Frank loops [28], preventing the motion of dislocations thus leading to hardening, and also reducing strain-hardening capabilities. To account for those effects, a crystal plasticity constitutive model developed in [20, 21] is described, with the dislocation and Frank loop density-based evolution laws.

To describe the plastic behaviour of single crystalline material, in general two laws are considered: a shear flow law that activates a slip system and determines its slip rate, and a hardening law that describes the change of slip activation with applied slip by taking into account the evolution of various defects created

within the material. The shear flow adopted here for non-irradiated and irradiated conditions is of visco-plastic type and represents isotropic hardening,

$$\dot{\gamma}^\alpha = \left\langle \frac{|\tau^\alpha| - \tau_c^\alpha}{K_0} \right\rangle^n \text{sign}(\tau^\alpha), \quad \text{with} \quad \langle x \rangle = \begin{cases} x & ; x > 0 \\ 0 & ; x \leq 0 \end{cases} \quad (1)$$

where γ^α is shear strain in slip system α ($\alpha = 1 \dots 12$ for Face-Centered-Cubic lattice) and τ^α and τ_c^α are respectively the resolved shear stress and critical resolved shear stress. Parameters K_0 and n regulate the viscosity of the shear flow.

The critical resolved shear stress is additively decomposed into components that contribute to the hardening [29],

$$\tau_c^\alpha = \begin{cases} \tau_0 + \mu \sqrt{\sum_{\beta=1}^{12} a^{\alpha\beta} r_D^\beta} & ; \text{non-irradiated} \\ \tau_0 + \tau_a \exp\left(-\frac{|\gamma^\alpha|}{\gamma_0}\right) + \mu \sqrt{\sum_{\beta=1}^{12} a^{\alpha\beta} r_D^\beta} + \mu \alpha_L \sqrt{\sum_{p=1}^4 r_L^p} & ; \text{irradiated} \end{cases} \quad (2)$$

The hardening law for non-irradiated steels accounts only for dislocation density evolution. Here, r_D^α is normalized dislocation density in slip system α (normalization factor b_D^2 , with Burgers vector $b_D = 2.54 \cdot 10^{-10} \text{m}$), τ_0 is lattice friction stress that remains constant for a given temperature, while μ and $a^{\alpha\beta}$ are respectively the macroscopic shear modulus and 12×12 matrix (with 6 independent parameters) of long-range interactions between dislocations. In the irradiated material, additional hardening is expected due to the presence of Frank loops. Here, r_L^p is a normalized Frank loop density in slip plane p (normalization factor $b_L^2 \phi_L$, with Burgers vector $b_L = 2.08 \cdot 10^{-10} \text{m}$ and ϕ_L the mean size of Frank loops that depends on irradiation level, see [20]) and α_L sets the relative contribution of Frank loops to hardening. To account for a dislocation unlock mechanism [21, 20], the additional phenomenological term has been proposed along with a dose dependant shear stress τ_a required to unlock the dislocations and coefficient γ_0 to adjust the speed of the avalanche after unlocking the dislocations.

The evolution of dislocation density is modeled with a multiplication and an annihilation term [29],

$$\dot{r}_D^\alpha = \begin{cases} \left(\frac{1}{\kappa} \sqrt{\sum_{\beta=1}^{12} b^{\alpha\beta} r_D^\beta} - G_c r_D^\alpha \right) |\dot{\gamma}^\alpha| & ; \text{non-irradiated} \\ \left(\frac{1}{\kappa} \sqrt{\sum_{\beta=1}^{12} b^{\alpha\beta} r_D^\beta} + \frac{1}{\kappa} \sqrt{K_{dl} \sum_{p=1}^4 r_L^p} - G_c r_D^\alpha \right) |\dot{\gamma}^\alpha| & ; \text{irradiated} \end{cases} \quad (3)$$

where $b^{\alpha\beta}$ is a matrix of interactions between dislocations, being of the same shape as $a^{\alpha\beta}$. Parameter κ is proportional to the number of obstacles crossed by a dislocation before being immobilized and G_c is a proportional factor that depends on the annihilation mechanism of dislocation dipoles. The irradiation effects are modeled by adding a term to the multiplication part, with K_{dl} being a coefficient of effective interaction between dislocations and Frank loops.

The evolution of Frank loop density in irradiated steels is modeled by Eq. 4 proposed in [30]

$$\dot{r}_L^p = -A_L (r_L^p - r_L^{sat}) \left(\sum_{\alpha \in \text{plane } p}^3 r_D^\alpha \right) \left(\sum_{\alpha \in \text{plane } p}^3 |\dot{\gamma}^\alpha| \right) \quad (4)$$

where A_L is the annihilation dimensionless area (rescaling factor b_L^3 / ϕ_L) of Frank loops and r_L^{sat} is a stabilized value of normalized defect density which depends on the irradiation dose. Since scanning of Frank loops by

mobile dislocations occurs only within the plane of the loop, only slipping in this plane can contribute to the evolution of defect density ($\alpha \in \text{plane } p$).

Anisotropic elasticity is finally considered, with non-zero parameters of the elastic fourth order tensor $C_{11} = C_{22} = C_{33}$, $C_{12} = C_{13} = C_{23}$ and $C_{44} = C_{55} = C_{66}$ in Voigt notations.

C_{11}	199 GPa					
C_{12}	136 GPa					
C_{44}	105 GPa					
K_0	10 MPa		0 dpa	0.8 dpa	2 dpa	3.4 dpa
n	15					13 dpa
τ_0	88 MPa	r_D^0	$5.38 \cdot 10^{-11}$	$4.54 \cdot 10^{-11}$	$3.66 \cdot 10^{-11}$	$2.97 \cdot 10^{-11}$
μ	65615 MPa	r_L^0	-	$2.29 \cdot 10^{-6}$	$4.72 \cdot 10^{-6}$	$5.04 \cdot 10^{-6}$
G_c	10.4	α_L	-	0.21	0.44	0.49
κ	42.8	K_{dl}	-		$0.25 \cdot 10^{-6}$	0.57
a_1	0.124	A_L	-	-	$4.48 \cdot 10^8$	$5.62 \cdot 10^8$
a_2	0.124	r_L^{sat}	-	$2.29 \cdot 10^{-6}$	$3.78 \cdot 10^{-6}$	$3.98 \cdot 10^{-6}$
a_3	0.07	τ_a	-	-	50.0 MPa	61.3 MPa
a_4	0.625	γ_0	-		$5 \cdot 10^{-3}$	61.2 MPa
a_5	0.137					
a_6	0.122					
b_i	$1 - \delta_{i1}$					

Table 1. Parameters of the constitutive law for neutron-irradiated austenitic stainless steel SA304 at 330°C [20].

Parameters of the constitutive law have been determined by fitting a polycrystalline aggregate model response [21, 20] to tensile measurements on 304 stainless steel at 330°C [31]. This crystal plasticity model is able to reproduce tensile tests up to 13 dpa, as well as the evolution of dislocation and Frank loops densities as a function of strain and irradiation level. The parameters are summarized in Table 1.

2.2. Numerical implementations

The above constitutive law has been implemented into two numerical codes: Abaqus [32] and Cast3M [33] with different methods to assess robustness of numerical integration.

In both implementations finite strain is accounted for by the usual multiplicative decomposition of the deformation gradient,

$$F = F^e F^p. \quad (5)$$

The crystal deforms solely through plastic shearing on crystallographic slip systems from the reference configuration to an intermediate configuration by the plastic deformation gradient F^p . The elastic deformation gradient, F^e , then stretches and rotates the lattice to bring the crystal to the final configuration.

The evolution of F^p is given by the flow rule,

$$\dot{F}^p = L^p F^p \quad (6)$$

where L^p is the local velocity gradient assumed to arise only from the plastic shearing of individual slip systems of the crystal defined as

$$L^p = \sum_{\alpha=1}^{12} \dot{\gamma}^\alpha N^\alpha \quad \text{with} \quad N^\alpha = s^\alpha \otimes m^\alpha \quad (7)$$

and s_i^α being a vector lying along the slip direction and m_i^α a vector normal to the slip plane of system α .

The elastic strain measure is given by Green-Lagrange strain tensor,

$$E = \frac{1}{2} \left((F^e)^T F^e - I \right), \quad (8)$$

and the stress measure by Mandel stress tensor,

$$M = \det(F^e) (F^e)^T \sigma (F^e)^{-T}, \quad (9)$$

where σ is the true (Cauchy) stress. In this way, the resolved shear stress, τ^α , can be calculated as

$$\tau^\alpha = M : N^\alpha = M : (s^\alpha \otimes m^\alpha). \quad (10)$$

The two different methods used for numerical integration are briefly sketched in Appendix, focusing primarily on the integration of the internal variables. The differences between the two implementations are highlighted. Both implementations (Abaqus and Cast3M) have been shown to give equivalent results for different crystal orientations. In the following, results coming from these two different implementations will not be differentiated.

2.3. Polycrystalline aggregates

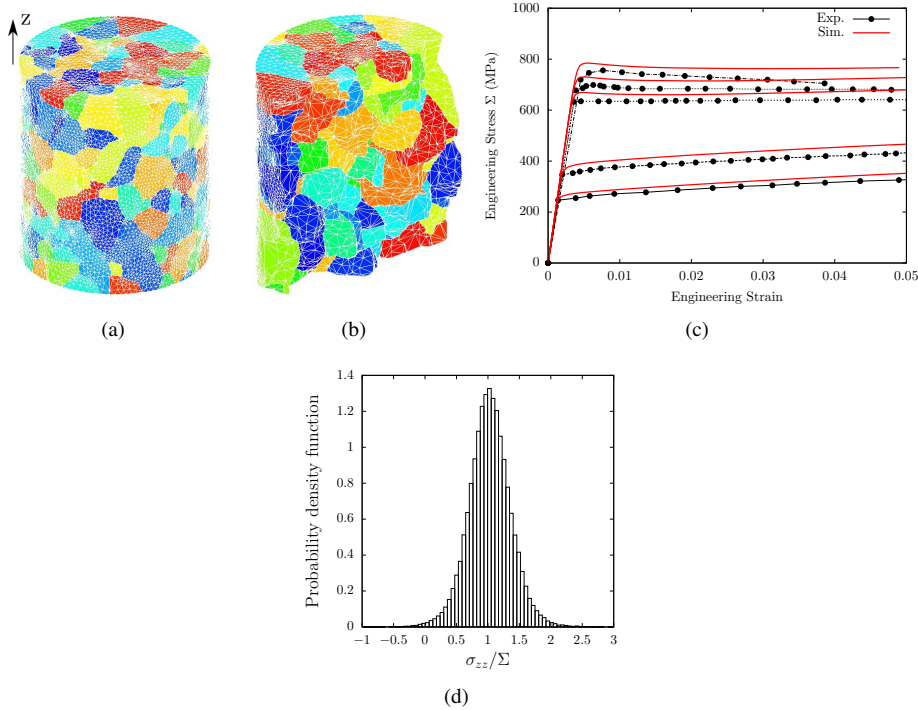


Figure 1. (a) The mesh used throughout this study, composed of 142k tetrahedral quadratic elements, has been obtained from X-ray Diffraction Contrast Tomography (DCT) on an austenitic stainless steel wire of $400\mu\text{m}$ diameter [34]. Each color correspond to a different grain, characterised by its crystallographic orientation also given by DCT. The wire is composed of 377 grains. (b) Details of the interior mesh of the wire. (c) Tensile Tests: Comparisons between experimental data (Exp.) and numerical simulations (Sim.) up to 5% total strain, for different levels of irradiation [0,0.8,2.3,4,13] dpa. (d) Typical distribution of axial stress in the aggregate.

Polycrystalline aggregate models are generated upon analytic and realistic grain structures. They are, respectively, built from Voronoi tessellations with random initial grain orientations and from diffraction contrast tomography data [35] of a stainless steel wire specimen (see, *e.g.*, Fig. 1a). The framework for building a finite element model of grains in realistic spatial structures is described in detail in [34]. In both cases, the grains have been assigned the material model introduced in Section 2.1 while the grain boundaries have not been modeled explicitly.

model	type	grains	elements	orientations
VORO – 216	analytic	216	38350	random
VORO – 343	analytic	343	64331	random
Wire coarse	realistic	377	141968	realistic
Wire fine	realistic	377	796105	realistic

Table 2. Finite element models of polycrystalline aggregates with the corresponding numbers of grains and elements. Initial crystallographic grain orientations are also shown. Note that random orientations provide no texture.

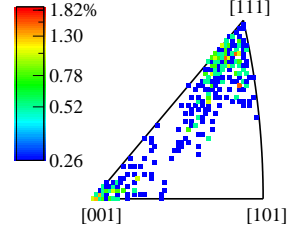


Figure 2. Inverse pole figure for rolling (tensile) model direction showing the initial distribution of the crystallographic orientations in the wire model. Colors denote a percentage of the grains in the model sharing the same pole value.

In all considered models the grains are meshed by quadratic tetrahedral elements. Two mesh densities are tested for each Voronoi and wire topology to estimate finite element size effects. In this respect, meshes with up to 64k and 800k elements have been used in the analyses for Voronoi and wire geometries, respectively (Tab. 2). Wire model shows crystallographic texture, as shown on Fig. 2.

Regarding boundary conditions, an incremental tensile displacement is applied along the axial (Z) axis to all the nodes on the top surface, while the nodes on the bottom surface are constrained to have zero axial displacement. Nodes on the lateral surface are not constrained so as to study the free surface effect. The applied nominal strain is $\Delta z/z_0 = 0.05$ and the strain rate is in the range $[10^{-4} - 10^{-3} \text{ s}^{-1}]^1$.

Figure 1(c) compares the calculated and measured engineering tensile curves on 304L stainless steel [31] at five levels of irradiation. Simulations are performed up to 5% plastic strain, as IGSCC initiation of irradiated stainless steel is usually observed close or below the yield stress. The curves show typical dose dependence for austenitic stainless steel [36]: with increasing irradiation the yield stress is also increased and a pronounced softening is observed just after the yield point at doses equal or higher than 2.0 dpa. The corresponding calculations have been performed on a wire model up to 0.05 strain using the material parameters from Table 1. A qualitatively good agreement with the experiment is observed for all doses. As macroscopic convergence with respect to the number of grains and mesh density is achieved for the wire model (see section 4), the slightly stiffer response at higher levels of irradiation can be attributed to the initial (as measured) texture of the wire which is a consequence of the manufacturing process. Distribution of axial stress in the aggregate is given in Fig. 1d, where a typical gaussian shape is obtained.

3. Intergranular normal stress distributions

Simulations performed on a wire austenitic stainless steel aggregate with physically-based crystal plasticity constitutive equations allow to obtain probability density functions (thereafter noted *pdf*) of normal

¹Parameters K_0 and n of the shear flow rule have been chosen such as to reproduce the weak viscous behaviour of austenitic stainless steel at 330°C [20], thus there is no effect of strain rate on stresses in the range used in this study.

stress σ_{mn} between adjacent grains as a function of strain and irradiation. As brittle cracking of grain boundaries is related to the level of normal stress, these pdf are believed to be a key ingredient towards IGSCC modelling. Results presented in this section correspond to the *coarse wire* finite element model. Parameters that may have an influence on intergranular normal stress distribution - such as free surface, crystallographic texture, grain shapes - are assessed in the next section.

For each pair of tetrahedral elements defining a boundary between two grains, the stress tensors $\underline{\sigma}$ at the closest Gauss points near the boundary are obtained, then converted to normal stresses knowing the normal \underline{n} of the grain boundary facet $\sigma_{mn} = \underline{n} \cdot \underline{\sigma} \cdot \underline{n}$, and finally averaged to yield a single value. It should be noted that the value of the intergranular normal stress strongly depends on the cosine of the angle between the normal to the grain boundary and the loading direction, which is almost uniformly distributed for the polycrystalline aggregates used in this study², and is bounded by the macroscopic uniaxial stress in the absence of mismatch effects between adjacent grains. As elements of different sizes are used in the mesh, the occurrence of σ_{mn} is weighted by the surface of the grain boundary facet on which it was obtained for the computation of the *pdf*. One may note however that such rescaling has only a small effect on the results.

The methodology used here to obtain intergranular normal stress differs from those used in [23] and [25]. In the former, additional Gauss points are considered in elements close to grain boundaries, while cohesive zone model elements are added to the model in the latter to obtain stresses precisely at grain boundaries. The rather simple method used in this study is however shown to be accurate enough to get the global shapes of the distributions in Section 4 upon refining mesh.

3.1. Effect of irradiation and strain level

Probability density functions of normal intergranular stress are shown on Fig. 3 as a function of irradiation level, at yield stress (Fig. 3a) and for a strain of 5% (Fig. 3b). The distributions have complex shapes, resulting from elastic and/or plastic incompatibilities between adjacent grains. One may note here that such shapes are not Gaussian, which means that using only standard deviation as done in other studies to describe them is not sufficient. The higher the macroscopic stress (yield stress increases with irradiation level, see Fig. 1c), the wider the pdf of normal intergranular stress, and the larger the upper tail of the distribution as can be seen on Fig. 3a. As the level of irradiation increases, the *pdf* flattens, and a significant probability (defined as the integral of the *pdf*) is always associated with stresses higher than the macroscopic value of the stress. The difference between unirradiated and irradiated material is reduced as the strain level increases, which may be related to the fact that the unirradiated material has more work-hardening capabilities than irradiated material, which tends to bring stress states closer for a given strain value.

²See inset Fig. 9b and Section 4.2 for discussion.

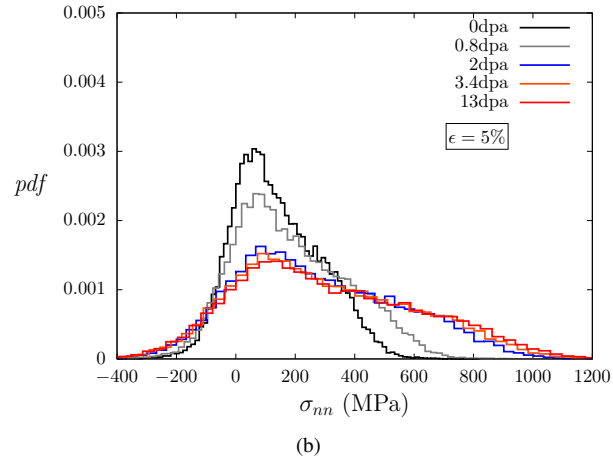
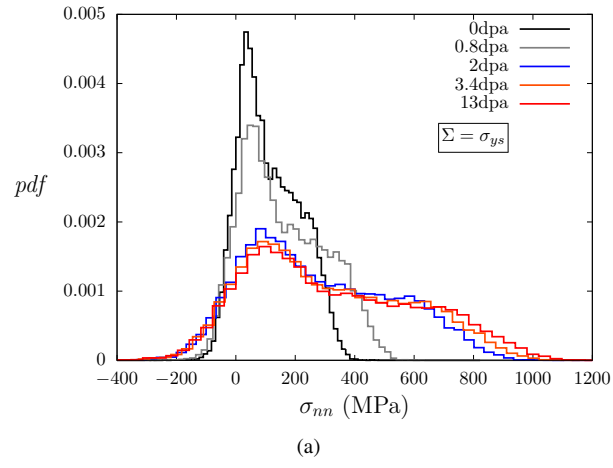


Figure 3. Probability density functions of intergranular normal stress σ_{nn} as a function of the level of irradiation, for (a) macroscopic yield stress and (b) a total strain of 5%.

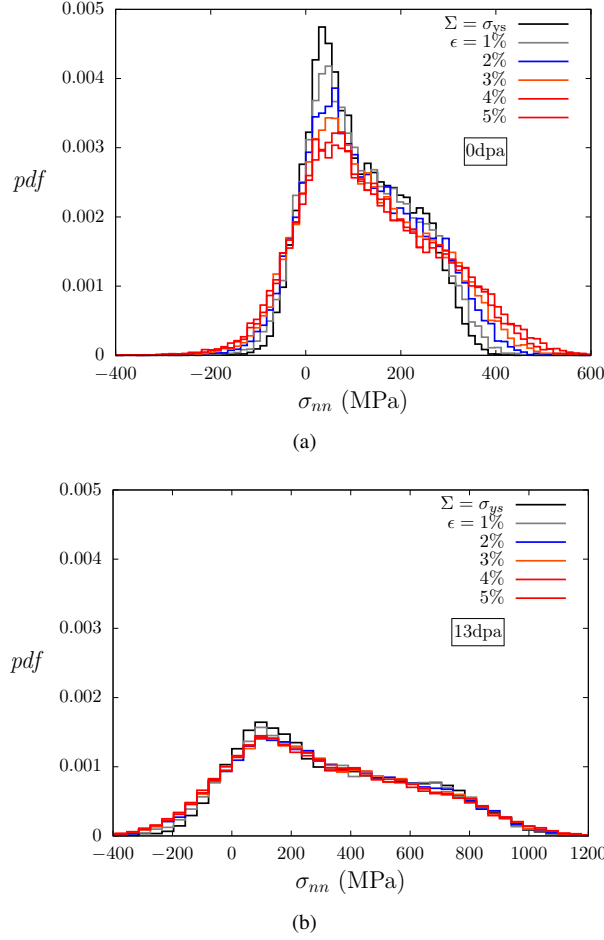


Figure 4. Probability density functions of intergranular normal stress σ_{nn} as a function of strain, for (a) unirradiated material (b) 13 dpa irradiated material.

In addition, for two different levels of irradiation, the evolution of the intergranular normal stress *pdf* with total strain is shown on Fig. 4. For the unirradiated material, the *pdf* flattens with work-hardening, while there are no changes for highly irradiated material that has almost no work-hardening capabilities, and thus no increase of the upper tail of distribution compared to unirradiated material.

3.2. Master curve

Rescaling all *pdfs* by the macroscopic uniaxial stress Σ at which they were obtained³, for all strains (yield strain-5%) and irradiation levels (0-13 dpa), leads at first order to a master curve shown on Fig. 5. This master curve appears to be well approximated by a mixture of two normal distributions

³For the relatively small values of global strain considered in this study, we do not differentiate engineering stress and true stress.

$$\text{pdf}\left(x = \frac{\sigma_{nn}}{\Sigma}\right) = \frac{a}{\sqrt{2\pi}\sigma_1} \exp\left[-\frac{(x - \mu_1)^2}{2\sigma_1^2}\right] + \frac{1-a}{\sqrt{2\pi}\sigma_2} \exp\left[-\frac{(x - \mu_2)^2}{2\sigma_2^2}\right] \quad (11)$$

with parameters $a = 0.51$, $\mu_1 = 0.67$, $\sigma_1 = 0.33$, $\mu_2 = 0.10$ and $\sigma_2 = 0.21$. Such kind of distribution of normal stress is found for example for the sum of an uniaxial stress tensor $\Sigma \underline{e}_3 \otimes \underline{e}_3$ and a fluctuation diagonal stress tensor, $\underline{\sigma} = \sigma_{imp}^1 \underline{e}_1 \otimes \underline{e}_1 + \sigma_{imp}^2 \underline{e}_2 \otimes \underline{e}_2 + (\Sigma + \sigma_{imp}^3) \underline{e}_3 \otimes \underline{e}_3$, assuming random normal orientations of the grain boundary facets, where σ_{imp}^i follows a normal distribution with zero mean. Such stress tensor can be seen as an approximation of stress at grain boundaries inside a polycrystalline aggregate in uniaxial tension, where σ_{imp}^i comes from incompatibilities of deformations between adjacent grains, which explains the shapes of distributions obtained throughout this study. Additional simulations have shown in fact that the shape of this master curve, and in particular the upper tail, remains practically unchanged when plasticity is omitted so that only elastic interactions are assumed between the grains, as simulations using only cubic elasticity (and no plasticity) give close results. However, for larger strains, significant deviations from cubic elasticity results are expected, but may not be relevant regarding IGSCC of post-irradiated materials where macroscopic stress is close or below the yield stress. For example, at constant load tests macroscopic stress is equal or below yield stress [6] and at constant extension rate tests strain is usually lower than few percents [27].

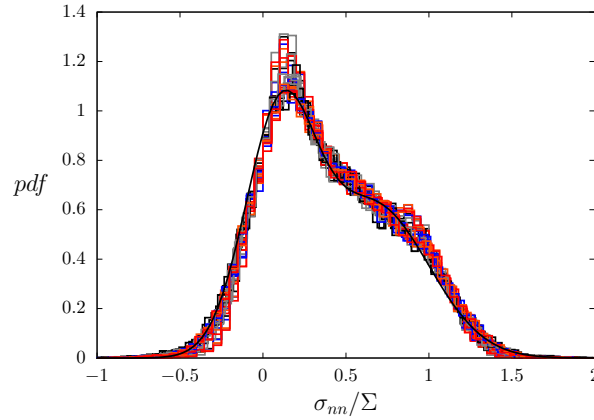


Figure 5. Probability density functions of intergranular normal stress σ_{nn} rescaled by macroscopic stress Σ . All curves, spanning 0 to 5% strain, and 0 to 13 dpa, are well approximated by a mixture of two normal distributions (Eq. 11) with parameters $a = 0.51$, $\mu_1 = 0.67$, $\sigma_1 = 0.33$, $\mu_2 = 0.10$ and $\sigma_2 = 0.21$ (black thick line).

In order that the probability density functions obtained in this study to be useful for IGSCC modelling, the dependence to the refinement of the mesh and grain number need to be assessed, which is done in the next section. Sensitivity to crystallographic texture, Grain shapes and to free surface is also studied to uncover the relevant parameters governing quantitatively the master curve, and especially the upper tail of the distributions which is relevant for IGSCC modelling from a statistical point of view.

4. Master curve parameters assessment

The results shown in Section 3 (referred to as *coarse wire*) are compared to the ones obtained with other aggregates presented in Table 2. Fine and coarse wires differ only by the refinement of the mesh and are

based on wire microstructure (both for the grain shapes and orientations, thus with crystallographic texture), while VORO-216 and VORO-343 are Voronoi tessellation based aggregates with different number of grains, with no crystallographic texture.

4.1. Grain number and mesh density

The macroscopic stress-strain curves for the four aggregates are shown on Fig. 6 for two levels of irradiation (0, 13dpa), and compared to experimental data on which the constitutive equations were calibrated [20]. Macroscopic convergence is achieved for the wire aggregates, and the results for Voronoi aggregates indicate that grain number convergence is achieved for 216 grains. All numerical curves are in reasonable agreement with the experimental data. Voronoi aggregates appear to be softer, which can be explained by the fact that the parameters of the constitutive law were adjusted in [20] on Voronoi models where the nodes on the lateral surfaces of the aggregate were imposed to move by the same amount. In this way, the interaction with the surrounding material was simulated to provide a bulk response. This kind of boundary conditions leads to harder mechanical response. Voronoi and Wire aggregates used here have same boundary conditions, the difference between the two arises from the difference in crystallographic texture as mentioned previously.

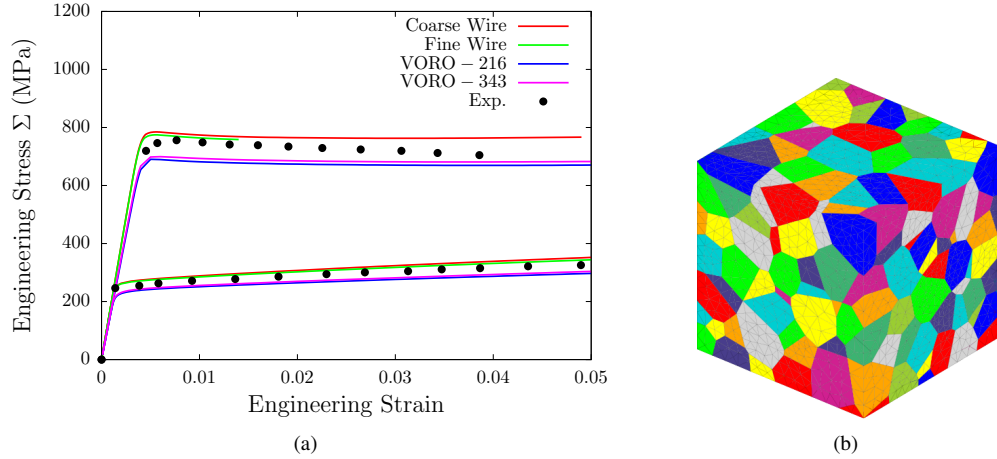
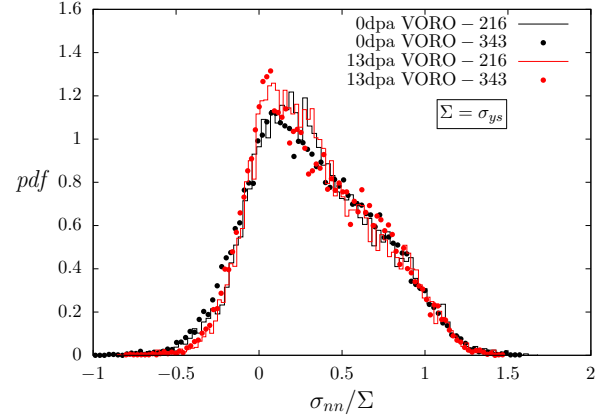
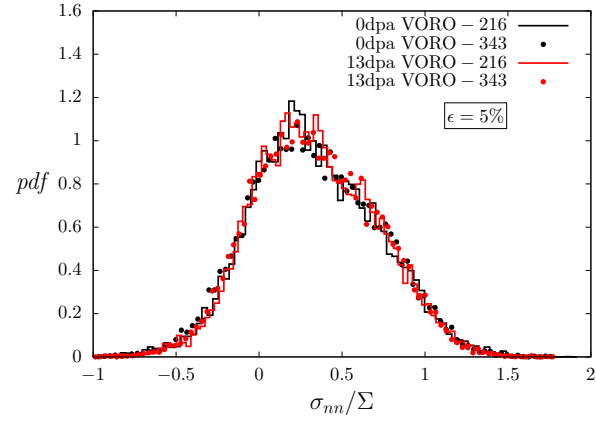


Figure 6. (a) Comparisons of macroscopic strain-stress curves between experimental data and numerical simulations for 0dpa and 13dpa. (b) Typical Voronoi aggregate mesh used in this study.

The local convergence with respect to the number of grains is shown on Fig. 7, where the probability density functions of intergranular normal stress are shown for different strain and irradiation levels. Simulations on the finer mesh for the wire aggregate (Fig. 8) show mesh convergence and also validate the methodology to compute stresses at grain boundaries.



(a)



(b)

Figure 7. Probability density functions of intergranular normal stress σ_{nm} rescaled by the macroscopic stress for Voronoi aggregates, for (a) yield stress (b) strain of 5%. Simulations with coarser mesh (not presented here) have confirmed the mesh convergence.

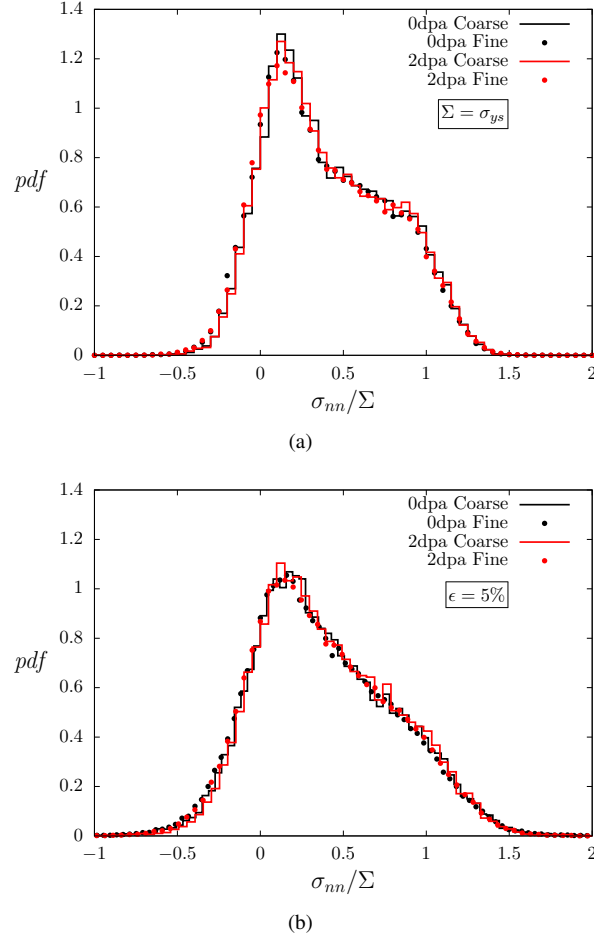


Figure 8. Probability density functions of intergranular normal stress σ_{nn} rescaled by the macroscopic stress for wire aggregates, for (a) yield stress (b) strain of 5%.

4.2. Texture and Grain shape effects

As previously mentioned, the wire exhibits a non-zero texture. Two regions of predominant crystallographic orientations are visible (Fig. 2), one close to [111] and the other close to [001] orientation. Such a finite (but small) texture is a consequence of the manufacturing process of the wire. To assess the influence of the texture, additional simulations were performed on the wire aggregate with random crystallographic orientations. As shown on Fig. 9a, significant deviations are observed, mainly close to zero stress, and thus full distributions depends significantly on crystallographic texture. However, the upper tail is left unchanged and appears to be relatively insensitive to small deviations from random orientations. In addition, results obtained on wire aggregate with random crystallographic orientations are compared to those obtained on Voronoi aggregates (Fig. 9b). Significant deviations are observed for the upper tail, wire aggregate showing larger intergranular stress than Voronoi aggregate. These are analysed further in the inset of Fig. 9b. A clear deviation from the uniform probability density distribution of the cosine of the angle, $\cos(\Theta)$, between the grain boundary normal and the loading direction observed in the wire suggests that grain boundary facets

that are parallel, $\cos(\Theta) \sim \pm 1$, or perpendicular, $\cos(\Theta) \sim 0$, to the two base surfaces of the wire are relatively more frequent. This kind of distribution of grain shapes in a realistic wire model also seems to be a consequence of the manufacturing process. As grain boundaries perpendicular to loading direction are more susceptible to generate large stress, the difference between Voronoi and wire aggregate is attributed to differences in grain shapes.

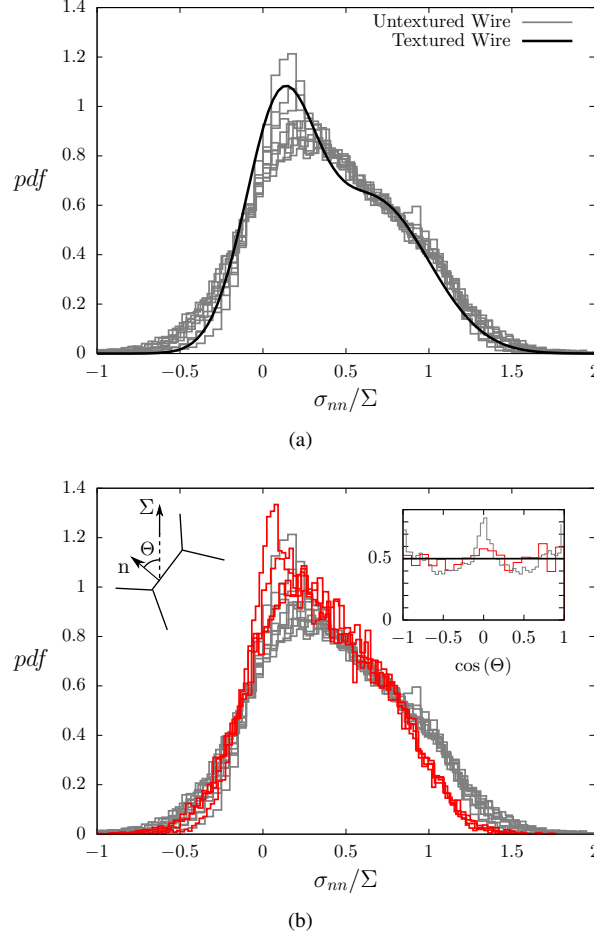


Figure 9. Comparisons of probability density functions of intergranular normal stress rescaled by macroscopic stress (a) obtained on wire model with random crystallographic orientations (solid gray lines) to the master curve (black line) obtained for original wire aggregate (b) of wire model with random crystallographic orientations (solid gray lines) to voronoi model (red lines) for different levels of strain and irradiation. Inset: Probability density function of the cosine of the angle between the grain boundary normal and the loading direction, for a typical Voronoi aggregate (red line), coarse wire aggregate (gray line) compared to the theoretical prediction assuming random orientations (black line).

4.3. Free surface effect

All probability density functions presented here above were obtained after post-processing entire aggregates in uniaxial tension, *i.e.* independently of the location of the boundary between the two grains with respect to the distance from the free surface. As cracking coming from IGSCC phenomenon is a damage

process initiating at the surface, the *pdf* of intergranular normal stress close to the free surface have also been studied. Comparison between the master curve of Fig. 5 to *pdf* obtained on the wire aggregate by considering only grain boundaries close to the free surface is presented on Fig. 10.

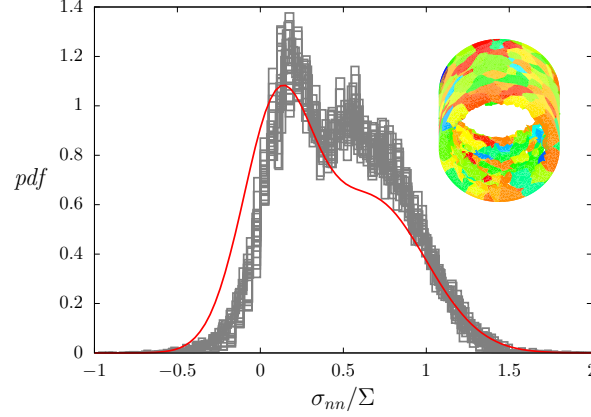


Figure 10. Comparison of probability density functions of intergranular normal stress rescaled by macroscopic stress for wire aggregate (solid red line, see Fig. 5, considering the entire aggregate) and restricting to grain boundaries close to the free surface ($r/R > 0.90$, where r is the radial coordinate and R the radius of the wire. Lines for various strain and irradiation levels are shown in gray.

Probability density functions are significantly altered when looking at the bulk or close to the free surface. However, the upper tail is not significantly changed. As cracking initiation prediction will mainly depend on the higher level of stress occurring on the sample, this figure indicates that results obtained in bulk aggregates provides a good description of stress distribution close to a free surface, and therefore be used to model IGSCC.

4.4. Intergranular normal stress vs. plastic incompatibilities

As discussed in section 3.2, the stress distributions obtained throughout this study up to 5% strain were found to be rather insensitive to the presence of plasticity, suggesting that in stainless steel both elastic and plastic anisotropies develop similar incompatibilities between the grains. In order to assess this observation more precisely, relation between normal intergranular stress and plastic slip at grain boundary is computed. First, cumulative total plastic slip is presented on Fig. 11 at different irradiation levels for a given strain, showing large variations due to orientation of the grains with respect to the loading direction. At a given total strain, the homogeneity of plastic slip activity is reduced with irradiation, increasing material volumes that do not strain at all (blue regions in Fig. 11).

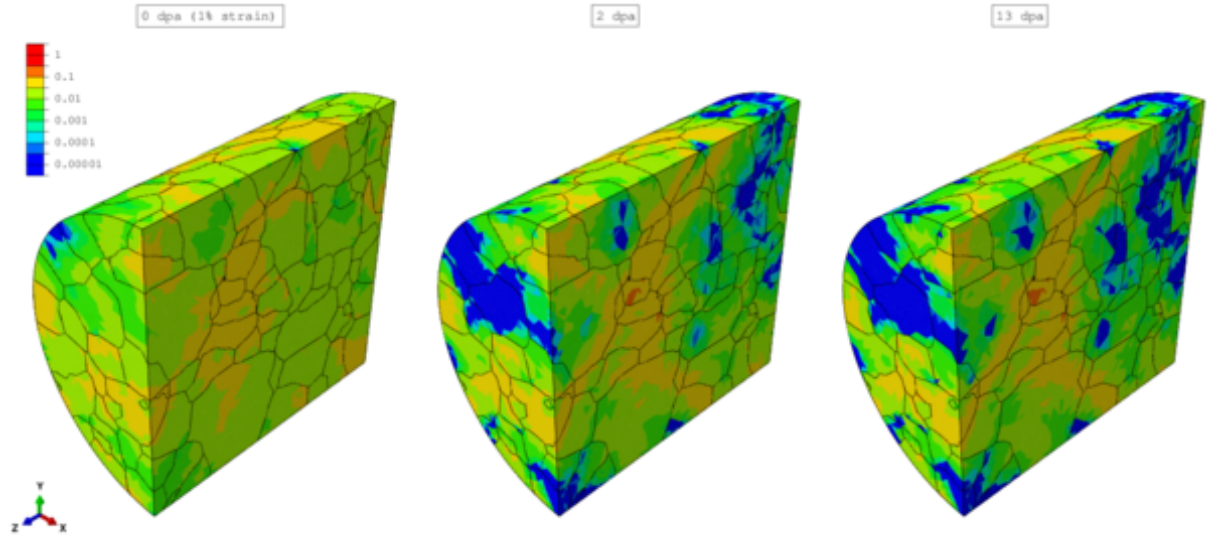
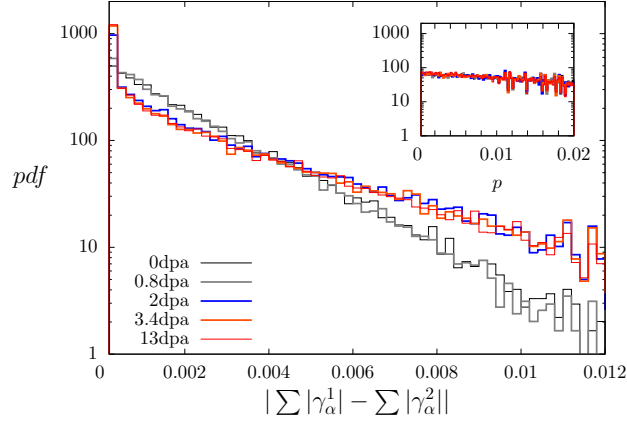


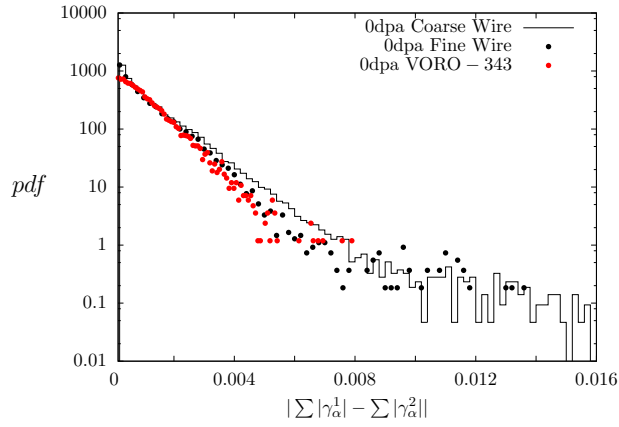
Figure 11. Comparison of the amount of plastic slip (as measured by $\sum_{\alpha} |\gamma_{\alpha}|$) for 1% strain for different irradiation levels. Half of the wire is omitted to visualize better the interior slip distribution. Logarithmic scale is used in the legend.

Plastic strain incompatibilities between adjacent grains are measured through the difference of cumulative plastic slips (defined as $\sum_{\alpha} |\gamma_{\alpha}|$) at grain boundaries⁴ and shown on Fig. 12. While some differences may be observed at yield stress for the different irradiation levels (Fig. 12a), distributions tend to become similar at higher strains (inset Fig. 12a). These distributions were observed to be rather insensitive to mesh and details of the microstructure.

⁴On each side of the grain boundary, cumulative plastic slip is computed on the closest Gauss points.



(a)



(b)

Figure 12. (a) Probability density functions of difference of cumulative plastic slips at grain boundaries at macroscopic yield stress (Inset: for 5% total strain), for different irradiation levels for wire aggregate (b) Probability density functions of difference of cumulative plastic slips at grain boundaries at macroscopic yield stress for unirradiated material. Comparison between wire and Voronoi aggregates.

Finally, 2D probability density functions of intergranular normal stress vs. of plastic slips discontinuities are shown on Fig. 13. With the constitutive equations and for the strain level used in this study, there is no correlation between high intergranular normal stress and high plastic slips discontinuities.

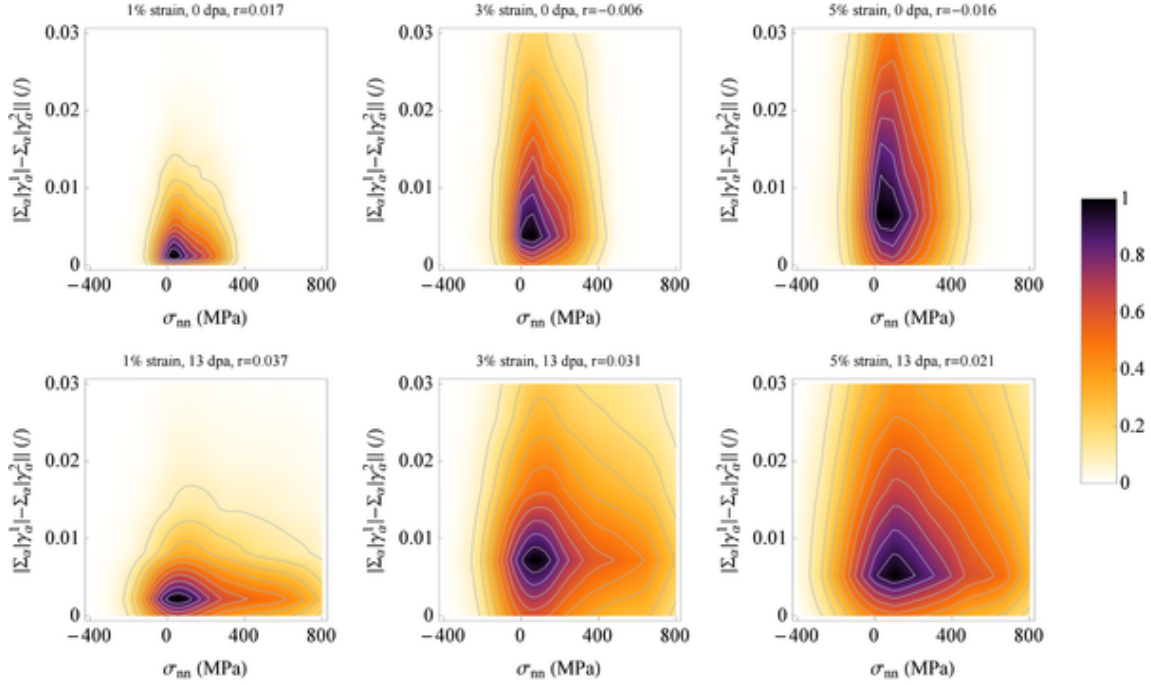


Figure 13. 2D probability density functions of intergranular stress vs. plastic slips discontinuities, for unirradiated and irradiated (13dpa) material, for three different levels of strain (1%, 3% and 5%). Small linear correlation coefficients, r , indicate a vanishing correlation between the two quantities.

5. Discussion

Predicting IGSCC of post-irradiated stainless steels requires evaluation of local stresses at grain boundaries. Finite-element simulations have been performed in this study on a realistic aggregate and using crystal plasticity constitutive equations calibrated for irradiated stainless steel to compute probability density functions of intergranular normal stresses at grain boundaries. As intergranular normal stresses used to compute probability density functions were weighted by the surface of the boundary on which they were obtained, the probability to have stress σ_{nn} higher than a given threshold σ_c : $P(\sigma_{nn} \geq \sigma_c) = \int_{\sigma_c}^{+\infty} pdf(\sigma_{nn})d\sigma_{nn}$ also corresponds to the percentage of surface of grain boundaries subjected to a stress higher than σ_c , and also approximately to the percentage of grain boundary length at the free surface subjected to a stress higher than σ_c , as shown on Fig. 10 for sufficiently high σ_c . Application of these distributions to the modelling of IGSCC requires the determination of the strength of the grain boundary as a function of oxidation level and irradiation in LWR environment. Therefore, once critical stress for oxidised grain boundary in LWR environment would become available in the literature, uncoupled modelling of IGSCC based on the distributions obtained in this study would become available, by setting a critical fraction of fractured grain boundaries above which global fracture of the specimen considered is expected. Such uncoupled modelling has been for example used successfully in ductile fracture analysis based on critical void radius and Rice-Tracey law [37].

Numerous studies have been conducted in the recent past on IGSCC of (ion-irradiated) austenitic stainless steel, mainly with applied stress well above yield stress. It has been shown (see, *e.g.*, [38]) that dislocation channelling (or clear bands) resulting in strain localization at the grain scale may be a factor controlling

IGSCC of irradiated stainless steel. The constitutive equations used in this study do not display instabilities and subsequent strong strain localization at the grain scale, and therefore the results and methodology proposed in this study would probably show limitations when applied to highly strained materials. However, and despite the fact the stress at which clear bands appear is still a matter of debate, the results shown here are expected to be suitable for low macroscopic stress (up to yield stress) and/or low irradiation level, for which channelling dislocation mode is not prominent, or for highly sensitized grain boundary. This is supported by results shown in Fig. 13, showing no correlation between high intergranular stress and plastic slip incompatibilities, indicating that a stress-controlled failure mode could appear before large plastic incompatibilities, for sufficiently weak grain boundary.

6. Conclusion

IGSCC modelling of irradiated stainless steel requires evaluation of stress distributions at grain boundaries and their evolution with both strain and irradiation level. Normal stress distributions at grain boundaries for (un)-irradiated austenitic stainless steel have been provided based on finite elements simulations performed on realistic aggregates with recently proposed physically-based crystal plasticity constitutive equations. In the realistic aggregate a mesh is obtained from diffraction contrast tomography data of an austenitic stainless steel wire, that gives both grain shapes and crystallographic orientations. Crystal plasticity constitutive equations are based on physically-based modelling, and have been adjusted so as to reproduce both macroscopic tensile tests and microscopic evolution of microstructure variables (dislocations and defects densities).

Once rescaled by the macroscopic stress, the distributions obtained are found to be well approximated by a master curve in the range [0-13 dpa] and [yield-5% strain]. The upper tail of this master curve, relevant for IGSCC initiation modelling, does not depend strongly on the crystallographic texture of the material close to random orientations, but is sensitive to grain shapes. This implies that realistic aggregates are required to obtain relevant intergranular stress distributions. In addition, free surface effect does not affect significantly the distributions of upper tail, thus allowing to use the distributions obtained in this study to describe intergranular stress at the free surface, which is relevant for IGSCC initiation. Based on these results, a methodology for uncoupled modelling of IGSCC of irradiated materials has been proposed and anticipated to provide reliable estimations for low strain and sufficiently weak grain boundaries, which are expected to be encountered in highly irradiated stainless steels.

Acknowledgments

The authors acknowledge the financial support from Slovenian Research Agency and French Atomic Energy Commission through the bilateral project Comprehensive and reliable prediction of LWRs internals mechanical behaviour based on microstructure-informed modeling between CEA and JSI in years 2013-2014. J.H would like to thank Chao Ling, Thomas Helfer and Lionel Gélébart for fruitful discussions and technical assistance in finite element simulations.

7. Appendix

7.1. Abaqus implementation

The implementation of constitutive equations in ABAQUS is done through a user-material subroutine UMAT [32]. Following Huang's implementation [39], large deformation theory is used along with forward gradient time integration scheme (θ method) and linear incremental formulation. The implementation results in a semi-implicit scheme. Detailed formulation of the implementation can be found in [40].

A time integration scheme assumes a linear relation among the increments of stresses, strains and internal variables such as shear strains, dislocation densities and irradiation defect (Frank loop) densities. The stresses and internal variables, $v \in \{\gamma^\alpha, r_D^\alpha, r_L^p\}$, are evaluated at the start of the increment so that

$$v_{t+\Delta t} = v_t + \Delta v_t \quad (12)$$

where the increment of the internal variable v within the time increment Δt is defined as

$$\Delta v_t = v(t + \Delta t) - v(t) = \Delta t ((1 - \theta)\dot{v}_t + \theta\dot{v}_{t+\Delta t}). \quad (13)$$

A parameter θ , ranging from 0 to 1, is introduced to employ a linear interpolation within Δt . A value of $\theta = 0$ corresponds to explicit Euler time integration scheme and $\theta > 0$ to semi-implicit one. A choice of θ between 0.5 and 1 is recommended [39].

A time derivative at $t + \Delta t$ is further approximated by applying the first-order Taylor expansion

$$\dot{v}_{t+\Delta t} = \dot{v}_t + \sum_i \frac{\partial \dot{v}}{\partial x_i} \Delta x_i \quad (14)$$

where partial derivatives are taken with respect to all time-dependent variables x_i that influence v , and Δx_i is the corresponding increment within Δt . In Eq. (1), for example, two variables apply, $x_1 = \tau^\alpha$ and $x_2 = \tau_c^\alpha$. Rearranging the above equations Eqs. (13 – 14) gives the following incremental relation

$$\Delta v_t = \Delta t \left(\dot{v}_t + \theta \sum_i \frac{\partial \dot{v}}{\partial x_i} \Delta x_i \right). \quad (15)$$

All partial derivatives in incremental relations for Δv_t can be explicitly derived from constitutive relations, Eqs. (1 – 4), and evaluated at the start of the increment. Also, each Δx_i may be expressed as a linear function of the increments $\Delta \gamma^\alpha, \Delta r_D^\alpha, \Delta r_L^p$ and strain increment $\Delta \varepsilon_{ij}$ [40]. In this way, a linear system of equations can be set up for the 28 unknowns $\Delta \gamma^\alpha, \Delta r_D^\alpha, \Delta r_L^p$. The solution for the increments is obtained by finding the inverse of the 28×28 matrix using the standard LU decomposition with Gauss elimination.

7.2. Cast3M implementation

Numerical simulations performed in Cast3M use a fully implicit implementation of the constitutive equations generated by the MFront code generator [41]. The implicit scheme assumes that stresses, strains and all internal variables, $v \in \{E^{ij}, \gamma^\alpha, r_D^\alpha, r_L^p\}$, are evaluated at the end of time increment, $t + \Delta t$, so that

$$v_{t+\Delta t} = v_t + \Delta v_{t+\Delta t}. \quad (16)$$

Note that elastic Green-Lagrange strain tensor E is considered here as additional free internal variable to avoid the risk of inaccuracy in the numerical calculation of the elastic and plastic part of deformation gradient, F^e and F^p [21]. The elastic part of the deformation at the end of the time step is approximated by the formula

$$F_{t+\Delta t}^e = \Delta F F_t^e (\Delta F^p)^{-1} \quad \text{with} \quad (\Delta F^p)^{-1} \approx \frac{1 - \sum_{\alpha=1}^{12} \Delta \gamma^\alpha N^\alpha}{\left[\det \left(1 - \sum_{\alpha=1}^{12} \Delta \gamma^\alpha N^\alpha \right) \right]^{1/3}} \quad (17)$$

using a multiplicative decomposition of the deformation gradient, $F = F^e F^p$, and $\Delta F = F_{t+\Delta t} F_t^{-1}$. To integrate internal variables at $t + \Delta t$, a nonlinear system of equations is solved by a Newton-Raphson iteration method. In this respect, vanishing residual functions, $R_{E^{ij}}, R_{\gamma^\alpha}, R_{r_D^\alpha}, R_{r_L^p}$, are defined by the evolution relations, Eqs. (1 – 4), and from Eq. (17),

$$\begin{aligned} R_{E^{ij}} &= \Delta E^{ij} + E_t^{ij} - \frac{1}{2} \left({}^t F_{t+\Delta t}^e F_{t+\Delta t}^e - 1 \right) \\ R_{\gamma^\alpha} &= \Delta \gamma^\alpha - \left\langle \frac{|\tau^\alpha| - \tau_c^\alpha}{K_0} \right\rangle^n \text{sign}(\tau^\alpha) \Delta t \\ R_{r_D^\alpha} &= \Delta r_D^\alpha - \begin{cases} \left(\frac{1}{\kappa} \sqrt{\sum_{\beta=1}^{12} b^{\alpha\beta} r_D^\beta} - G_c r_D^\alpha \right) |\Delta \gamma^\alpha| & ; \text{non-irradiated} \\ \left(\frac{1}{\kappa} \sqrt{\sum_{\beta=1}^{12} b^{\alpha\beta} r_D^\beta} + \frac{1}{\kappa} \sqrt{K_{dl} \sum_{p=1}^4 r_L^p} - G_c r_D^\alpha \right) |\Delta \gamma^\alpha| & ; \text{irradiated} \end{cases} \\ R_{r_L^p} &= \Delta r_L^p + A_L (r_L^p - r_L^{sat}) \left(\sum_{\alpha \in \text{plane } p}^3 r_D^\alpha \right) \left(\sum_{\alpha \in \text{plane } p}^3 |\Delta \gamma^\alpha| \right). \end{aligned} \quad (18)$$

References

- [1] O. Chopra, A. Rao, A review of irradiation effects on LWR core internal materials - Neutron embrittlement, J. Nuc. Mat. 412 (2011) 195–208.
- [2] O. Chopra, A. Rao, A review of irradiation effects on LWR core internal materials - IASCC susceptibility and crack growth rates of austenitic stainless steels, J. Nuc. Mat. 409 (2011) 235–256.
- [3] K. Fukuya, Current understanding of radiation-induced degradation in light water reactor structural materials, J. Nuc. Sci. and Tech. 50 (2013) 213–254.
- [4] IAEA, Stress corrosion cracking in light water reactors: Good practices and lessons learned, NP-T-3.13, IAEA Nuclear Energy Series (2011).
- [5] A. Hojna, Irradiation-assisted stress corrosion cracking and impact on life extension, Corrosion 69 (2013) 964–974.
- [6] P. Freyer, T. Mager, M. Burke, Hot cell crack initiation testing of various heats of highly irradiated 316 stainless steel components obtained from three commercial PWRs, in: 13th International Conference on Environmental Degradation of Materials in Nuclear Power Systems - Water Reactors, 2007.
- [7] J. Conermann, R. Shogan, K. Fojimoto, T. Yonezawa, Y. Yamaguchi, Irradiation effects in a highly irradiated cold worked stainless steel removed from a commercial PWR, in: 12th International Conference on Environmental Degradation of Materials in Nuclear Power Systems - Water Reactors, 2005.

- [8] K. Takakura, K. Nakata, M. Ando, K. Fujimoto, E. Washi, Lifetime evaluation for IASCC initiation of cold worked 316 stainless steels' BFB in PWR primary water, in: 13th International Conference on Environmental Degradation of Materials in Nuclear Power Systems - Water Reactors, 2007.
- [9] H. Nishioka, K. Fukuya, K. Fujii, T. Torimaru, IASCC initiation in highly irradiated stainless steels under uniaxial constant load conditions, *J. Nuc. Sci. and Tech.* 45 (2008) 1072–1077.
- [10] K. Stephenson, G. Was, Crack initiation behavior of neutron irradiated model and commercial stainless steels in high temperature water, *J. Nuc. Mat.* 444 (2014) 331–341.
- [11] R. Katsura, J. Morisawa, M. Kodama, S. Nishimura, S. Suzuki, S. Shima, M. Yamamoto, Effect of stress on IASCC in irradiated austenitic stainless steels, in: 6th International Conference on Environmental Degradation of Materials in Nuclear Power Systems - Water Reactors, 1993.
- [12] K. Fujii, H. Nishioka, K. Fukuya, T. Torimaru, Effects of dissolved hydrogen on IASCC behavior, in: Fontevraud 7: Contribution of Materials Investigations to Improve the Safety and Performance of LWRs, 2010.
- [13] M. Sauzay, M. Ould Moussa, Prediction of grain boundary stress fields and microcrack initiation induced by slip impingement, *Int. J. Fracture* 184 (2013) 215–240.
- [14] I. Simonovski, L. Cizelj, Cohesive zone modeling of intergranular cracking in polycrystalline aggregates, *Nuc. Eng. Design* 283 (2015) 139–147.
- [15] A. Musienko, G. Cailletaud, Simulation of inter- and transgranular crack propagation in polycrystalline aggregates due to stress corrosion cracking, *Acta Mat.* 57 (2009) 3840–3855.
- [16] T. Couvant, J. Proix, A. Seyeux, Modeling intergranular stress corrosion cracking of austenitic alloys exposed to PWR primary water, in: European Corrosion Congress, ISBN:978-989-98850-0-4, 2013.
- [17] S. De, Multiscale modeling of irradiated polycrystalline FCC metals, *Int. J. Solids and Structures* 51 (2014) 3919–3930.
- [18] X. Xiao, D. Song, J. Xue, H. Chu, H. Duan, A size-dependent tensorial plasticity model for FCC single crystal with irradiation, *Int. J. Plasticity* 65 (2015) 152–167.
- [19] N. Barton, J. Arsenlis, A. Ansarian, A polycrystal plasticity model of strain localization in irradiation iron, *J. Mech. Phys. Solids* 61 (2013) 341–351.
- [20] B. Tanguy, X. Han, J. Besson, S. Forest, C. Robertson, N. Rupin, Dislocations and irradiation defects-based micromechanical modelling for neutron irradiated austenitic stainless steels, Vol. International Symposium on Plasticity 2013 and Its Current Applications, 2013.
- [21] X. Han, Modélisation de la fragilisation due au gonflement dans les aciers inoxydables austénitiques irradiés, Ph.D. thesis, Ecole Nationale Supérieure des Mines de Paris (2012).
- [22] S. El Shawish, L. Cizelj, I. Simonovski, Modeling grain boundaries in polycrystals using cohesive elements: Qualitative and quantitative analysis, *Nuc. Eng. Des.* 261 (2013) 371–381.
- [23] O. Diard, S. Leclercq, G. Rousselier, G. Cailletaud, Distribution of normal stress at grain boundaries in multicrystals: application to an intergranular damage modeling, *Comp. Mat. Sci.* 25 (2002) 73–84.

- [24] O. Diard, S. Leclercq, G. Rousselier, G. Cailletaud, Evaluation of finite element based analysis of 3D multicrystalline aggregates plasticity application to crystal plasticity model identification and the study of strain fields near grain boundaries, *Int. J. Plasticity* 21 (2005) 691–722.
- [25] D. Gonzalez, I. Simonovski, P. Withers, J. Quinta da Fonseca, Modelling the effect of elastic and plastic anisotropies on stresses at grain boundaries, *Int. J. Plasticity* 61 (2014) 49–63.
- [26] O. Raquet, E. Herms, F. Vaillant, T. Couvant, SCC of cold-worked austenitic stainless steels in PWR conditions, *Adv. Mat. Sci.* 7 (2007) 33–46.
- [27] M. Le Millier, O. Calonne, J. Crépin, C. Duhamel, L. Fournier, F. Gaslain, E. Héripré, O. Toader, Y. Vidalenc, G. Was, Influence of strain localization on IASCC of proton irradiated 304L stainless steel in simulated PWR primary water, in: 16th International Conference on Environmental Degradation of Materials in Nuclear Power Systems - Water Reactors, 2013.
- [28] M. Victoria, N. Baluc, C. Bailat, Y. Dai, M. I. Luppó, R. Schublin, B. N. Singh, The microstructure and associated tensile properties of irradiated FCC and BCC metals, *J. Nucl. Mat.* 276 (2000) 114–122.
- [29] H. Mecking, U. Kocks, Kinetics of flow and strain-hardening, *Acta Metall.* 29 (1981) 1865–1875.
- [30] S. Krishna, S. De, A temperature and rate-dependent micromechanical model of molybdenum under neutron irradiation, *Phil. Mag.* 90 (2010) 4013–4025.
- [31] C. Pokor, Y. Bréchet, P. Dubuisson, J. P. Massoud, A. Barbu, Irradiation damage in 304 and 316 stainless steels: experimental investigation and modeling. part I: Evolution of the microstructure, *J. Nucl. Mat.* 326 (2004) 19–29.
- [32] Simulia, ABAQUS 6.13-4 (2014).
- [33] www-cast3m.com.
- [34] I. Simonovski, L. Cizelj, Automatic parallel generation of finite element meshes for complex spatial structures, *Comp. Mat. Science* 50 (2011) 1606–1618.
- [35] A. King, G. Johnson, D. Engelberg, W. Ludwig, J. Marrow, Observations of intergranular stress corrosion cracking in a grain-mapped polycrystal, *Science* 321 (2008) 382–385.
- [36] E. H. Lee, T. S. Byun, J. D. Hunn, K. Farrell, L. K. Mansur, Origin of hardening and deformation mechanisms in irradiated 316 In austenitic stainless steel, *J. Nucl. Mat.* 296 (2001) 183–191.
- [37] J. Besson, Continuum models of ductile fracture: a review, *Int. J. Damage Mechanics* 19 (2010) 3–52.
- [38] M. McMurtrey, B. Cui, I. Robertson, D. Farkas, G. Was, Mechanism of dislocation channel-induced irradiation assisted stress corrosion crack initiation in austenitic stainless steel, *Cur. Op. Solid State Mat. Sci.* 19 (2015) 305–314.
- [39] Y. Huang, User-material subroutine incorporating single crystal plasticity in the abaqus finite element program, Technical report, Division of Applied Sciences, Harvard University (1991).
- [40] S. El Shawish, L. Cizelj, B. Tanguy, X. Han, J. Hure, Extended crystal plasticity finite element approach for neutron irradiated austenitic stainless steels, in: 23rd International Conference Nuclear Energy for New Europe, September 8-11, 2014, Portorož, Slovenia, 2014.

- [41] T. Helfer, B. Michel, J. Proix, M. Salvo, J. Sercombe, M. Casella, Introducing the open-source mfront code generator: Application to mechanical behaviors and materials knowledge management within the PLEIADES fuel element modelling platform, *Comp. Math. with Applications* 70 (2015) 994–1023.